ACS NANO

www.acsnano.org

ARTICLE

Spectroscopic and Magneto-Optical Signatures of Cu^{1+} and Cu^{2+} Defects in Copper Indium Sulfide Quantum Dots

Addis Fuhr, Hyeong Jin Yun, Scott A. Crooker, and Victor I. Klimov*

Cite This: *ACS Nano* 2020, 14, 2212–2223

Read Online

ACCESS | Metrics & More | Article Recommendations | Supporting Information

ABSTRACT: **Colloidal quantum dots (QDs) of I–III–VI ternary compounds such as copper indium sulfide (CIS) and copper indium selenide (CISe) have been under intense investigation due to both their unusual photophysical properties and considerable technological utility. These materials feature a toxic-element-free composition, a tunable bandgap that covers near-infrared and visible spectral energies, and a highly efficient photoluminescence (PL) whose spectrum is located in the reabsorption-free intragap region. These properties make them attractive for light-emission and light-harvesting applications including photovoltaics and luminescent solar concentrators. Despite a large body of literature on device-related studies of CISe(S) QDs, the understanding of their fundamental photophysical properties is surprisingly poor. Two particular subjects that are still heavily debated in the literature include the mechanism(s) for strong intragap emission and the reason(s) for a poorly defined (featureless) absorption edge, which often "tails" below the nominal bandgap. Here, we address these questions by conducting comprehensive spectroscopic studies of CIS QD samples with varied Cu-to-In ratios using resonant PL and PL excitation, femtosecond transient absorption, and magnetic circular dichroism measurements. These studies reveal a strong effect of stoichiometry on the concentration of Cu^{1+} *vs* Cu^{2+} defects (occurring as Cu_{In}'' and $Cu_{Cu}^{\bullet}$ species, respectively), and their effects on QD optical properties. In particular, we demonstrate that the increase in the relative amount of Cu^{2+} *vs* Cu^{1+} centers suppresses intragap absorption associated with Cu^{1+} states and sharpens band-edge absorption. In addition, we show that both Cu^{1+} and Cu^{2+} centers are emissive but are characterized by distinct activation mechanisms and slightly different emission energies due to different crystal lattice environments. An important overall conclusion of this study is that the relative importance of the Cu^{2+} *vs* Cu^{1+} emission/absorption channels can be controlled by tuning the Cu-to-In ratio, suggesting that the control of sample stoichiometry represents a powerful tool for achieving functionalities (*e.g.*, strong intragap emission) that are not accessible with ideal, defect-free materials.**

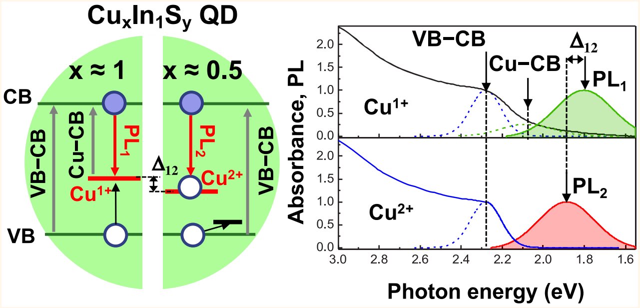

KEYWORDS: *copper indium sulfide, quantum dot, native defects, Cu^{1+}, Cu^{2+}, copper vacancy*

Colloidal nanocrystal quantum dots (QDs) of ternary $CuInS_2$ and $CuInSe_2$ (CIS and CISe, respectively) semiconductors and their quaternary alloys ($CuInS_{2-x}Se_x$ or CISeS) have received considerable attention as environmentally benign alternatives to more traditional QDs of heavy metal (Cd and Pb) based compositions.[1−15] In particular, CISeS QDs have been used to demonstrate high-performance optical, electronic, and optoelectronic devices including solar cells,[1,16−22] luminescence solar concentrators (LSCs),[23−28] light-emitting diodes,[29−31] biolabels,[3,32] and field-effect transistors.[33−35] Despite a large body of literature demonstrating the practical utility of these materials, the current understanding of their photophysical properties is surprisingly poor. I–III–VI CIS(Se) semiconductors are close relatives of II–VI CdS(Se) materials and can be thought of as being derived from them by replacing pairs of 2+ Cd cations in the adjacent unit cells with 3+ (In) and 1+ (Cu) cations. As a result of this substitution, the semiconductor bandgap (E_g) shifts to near-infrared energies ($E_{g,bulk}$ = 1.52 and 1.05 eV for bulk CIS and CISe, respectively).[36−38] Otherwise, macroscopic II–VI CdS(Se) and I–III–VI CIS(Se) crystals are characterized by similar optical properties. In particular, both families

Received: November 19, 2019
Accepted: January 13, 2020
Published: January 13, 2020

https://dx.doi.org/10.1021/acsnano.9b09181
ACS Nano 2020, 14, 2212–2223

of materials are direct-gap semiconductors and exhibit pronounced excitonic features in low-temperature emission and absorption spectra.[36−38]

Despite the similarities observed for their bulk forms, CIS(Se) and CdS(Se) exhibit vastly different optical behaviors when prepared as colloidal QDs. The peculiarities of CIS(Se) QD photophysics include an unusually large Stokes shift between the photoluminescence (PL) band and the absorption onset (300−500 meV *vs* <100 meV in CdSe QDs), a strong PL broadening (>300 meV *vs* <100 meV in CdSe QDs), very long radiative lifetimes (100−500 ns *vs* ~20 ns in CdSe QDs), and a featureless indirect-semiconductor-like absorption edge. These properties have been often ascribed to the involvement of optically active intragap defects.[4,8,9,39−42] In particular, key spectroscopic observations can be explained by a phenomenological model wherein the PL originates not from the intrinsic QD exciton recombination but instead involves a deep hole-like defect state, which optically couples to the band-edge electron.[2,4,7−9,12,15,28,39−43] The surprising persistence of this defect across all reported CIS(Se) QD samples indicates that it is native to these materials. Furthermore, the strong similarity between optical and magneto-optical properties of CIS(Se) QDs and II−VI QDs intentionally doped with Cu ions suggests that this native defect is Cu-related, as was proposed in ref 41 on the basis of a side-by-side comparison of CIS, Cu−doped ZnSe, and CdSe QDs.

While presently there is a growing consensus that the PL in CIS(Se) QDs involves a delocalized conduction band (CB) electron and a hole localized on a copper cation, the details of the emission mechanism are still under discussion. In particular, it has been debated whether it involves optically active Cu-related defects or self-trapped excitons residing preferentially on the Cu lattice sites due to a highly localized character of valence band (VB) molecular orbitals of CIS(Se) QDs.[10,11] Uncertainties also exist in the case of the Cu-defect models. Specifically, it remains unclear whether the Cu defect responsible for intragap emission is in the 1+ or the 2+ oxidation state.[9,39−41,44] Both of these states are emissive; however, the details of the emission process are distinct. In particular, as the Cu^{1+} state has a filled d shell ($3d^{10}$), its "activation" requires the capture of a photoexcited VB hole, which then radiatively recombines with the CB electron (Figure 1a, left). On the other hand, the Cu^{2+} defect has the $3d^9$ configuration, which contains an electron vacancy in the 3d shell. This hole-like 3d state is immediately "emission ready" and can radiatively trap a CB electron without prior activation (Figure 1a, right).[39,41,44] In fact, a photoinjected VB hole is detrimental to the Cu^{2+} emission mechanism, as this hole competes with the 3d hole-like vacancy for the same CB electron. In particular, if not promptly removed from the VB, the photoexcited hole can suppress intragap emission either by capturing the CB electron *via* the radiative transition[39] or by serving as an energy acceptor in a three-particle nonradiative Auger process involving the CB−Cu^{2+} transition.[9] Therefore, a fast removal of the VB hole due to trapping at a non-Cu^{1+}-related defect (*e.g.*, Cu vacancy)[39] is required for observation of Cu^{2+} emission (Figure 1a, right).

The oxidation state of the Cu defect also affects the light absorption properties of the QDs. In particular, the Cu^{1+} defect is expected to be "absorption active" (*i.e.*, absorptive) as one of its 3d electrons can be optically excited into the CB state leaving the copper cation in the $3d^9$ configuration.[4,39] The Cu^{1+}−CB transition is therefore expected to lead to an

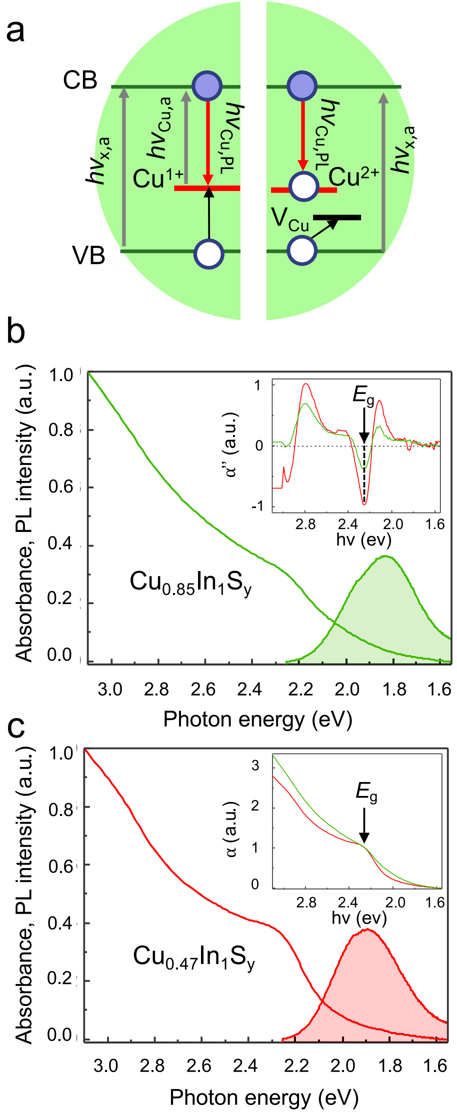

Figure 1. (a) Schematic depiction of band-edge optical transitions involved in PL (red arrows) and light absorption (gray arrows) in CIS QDs with Cu^{1+} (left) and Cu^{2+} (right) defects. In both cases, emission originates from the transition involving a CB electron and a hole-like intragap state localized on the Cu defect. In the case of the Cu^{1+} defect, activation of intragap PL occurs *via* trapping of a photogenerated VB hole by a negatively charged Cu_{In}'' center (black arrow in the left subpanel). On the other hand, the Cu^{2+} defect (occurs as a $Cu_{Cu}^{\bullet}$ center) is "emission ready" without prior activation. However, the observation of intragap emission in this case requires that the photogenerated hole is promptly removed from the VB state by trapping at, *e.g.*, a Cu vacancy (black arrow in the right subpanel). Otherwise, emission would be dominated by a much faster band-edge (CB−VB) transition. While both types of Cu defects are active in emission, only one of them (Cu^{1+}) leads to an additional near-band-edge feature in the absorption spectrum due to the intragap Cu^{1+}−CB transition (left subpanel). (b, c) Room-temperature absorption (lines) and emission (colored shading) spectra of CIS QDs with x = 0.85 (b) and 0.47 (c). Insets: The comparison of the second-derivative of the absorption spectra (α'') of these two samples (b) indicates that they are characterized by virtually identical bandgaps (E_g, inferred from the spectral position of the minimum of α''). The comparison of α-spectra normalized at $h\nu = E_g$ (c) indicates that the x = 0.85 sample exhibits a stronger intragap tail compared to the x = 0.47 sample.

https://dx.doi.org/10.1021/acsnano.9b09181
ACS Nano 2020, 14, 2212−2223

intragap absorption feature, which would contribute to the apparent broadening of the absorption edge (Figure 1a, left). The presence of the Cu^{2+} defects, on the other hand, does not lead to the development of additional intraband absorption features in the near-band-edge region, as the $3d^9$ configuration of the Cu ion cannot be optically transformed into the $3d^8$ state by promoting the 3d electron into the CB.[45] As a result, the Cu^{2+} defects are not expected to modify (broaden) the absorption edge (Figure 1a, right). Therefore, we will refer to these defects as "absorption-passive" or "nonabsorbing." We would like to point out, however, that while being optically passive in the upward transitions originating from the 3d shell, the $3d^9$ state of the Cu^{2+} ion can, in principle, be converted into the $3d^{10}$ configuration *via* an infrared optical transition whereby the VB electron is excited into the 3d state.[8]

Understanding the mechanisms underlying light−matter interactions in CIS(Se) QDs is critical to ongoing efforts to rationally control their optical and electro-optical functionalities for existing and emerging applications. One especially important question is whether the unusual photophysical behaviors of CIS(Se) QDs are intrinsic to these materials (as in the self-trapped exciton model[10,11]) or if they are derived from crystal imperfections (as in the "intragap-defect" models[2,4,7,9,12,15,39−43]). Further, if these properties are intrinsic, then why are they so different from those of either parental I−III−VI bulk crystals or structurally similar II−VI CdS(Se) QDs? On the other hand, if they are defect related, then why are they largely invariant from sample to sample? Finally, is it possible to control defect states to predictably modify the photophysical properties of CIS(Se) QDs?

Here, in order to answer these questions, we prepare $Cu_xIn_1S_y$ QDs with varied Cu-to-In ratios and elucidate the connection between sample stoichiometry and the abundance of specific defects and identify the corresponding implications for QD photophysical properties. In particular, on the basis of charge-compensation arguments, we expect that, in samples with a near stoichiometric, 1:1 Cu-to-In ratio, the prevailing defects are antisite $Cu_{In}''-In_{Cu}^{\bullet\bullet}$ pairs wherein the copper ion is in the 1+ oxidation state (here and later in this work, we use the Kröger−Vink notation of crystallographic defects).[46] On the other hand, increasing the degree of copper deficiency is anticipated to promote the formation of Cu vacancies (V_{Cu}'),[2,39] which in turn will facilitate the creation of charge compensating Cu^{2+} defects ($Cu_{Cu}^{\bullet}$). The results of magneto-optical measurements are consistent with this expected behavior. In particular, they reveal a systematic growth of the paramagnetic component of the magnetic circular dichroism (MCD) signal with the increasing degree of Cu deficiency, as expected for the increasing amount of paramagnetic spin-1/2 Cu^{2+} defects. The increased abundance of these species in Cu-deficient samples is also indicated by resonant PL, PL excitation (PLE), and transient absorption (TA) measurements. Furthermore, the conducted studies suggest that both Cu^{1+} and Cu^{2+} defects are emissive and characterized by close but distinguishable emission energies that reflect the distinct lattice environments of a Cu ion in the Cu_{In}'' and $Cu_{Cu}^{\bullet}$ states. In addition, we are able to quantify a true Stokes shift of intragap emission on the basis of its spectral displacement from the Cu^{1+} absorption band visualized *via* TA measurements. This quantity is distinct from the apparent Stokes shift defined as the displacement of the $Cu^{1+/2+}$ emission band from the intrinsic QD VB-to-CB absorption feature.

RESULTS AND DISCUSSION

Quantum Dot Samples. To experimentally elucidate the effect of sample stoichiometry on QD optical properties, we prepare and investigate $Cu_xIn_1S_y$ QDs with different Cu-to-In ratios (*i.e.*, different x values). In samples with the ideal stoichiometry ($x = 1$), $y = 2$; however, in non-stoichiometric samples, y can deviate from this ideal value. The samples were synthesized using 1-dodecanethiol and oleylamine as capping ligands (see the Methods and Experimental Section). The relative contents of Cu and In, determined by inductively coupled plasma atomic emission spectrometry (ICP-AES), were tuned by changing the molar ratio of the corresponding precursors. In our spectroscopic studies, we focus on two QD samples, one nearly stoichiometric ($x = 0.85$) and the other strongly copper deficient ($x = 0.47$).

Transmission electron microscopy (TEM) measurements indicate that QDs have a tetrahedral shape typical of nanocrystals with a chalcopyrite lattice (Figure S1). The chalcopyrite structure is also evident from the observed 3.2 Å spacing between adjacent crystal planes, which is consistent with the separation between the (112) planes of chalcopyrite $CuInS_2$ bulk crystals (Figure S1). The average QD size and size dispersion evaluated in terms of the length of a tetrahedra edge (L) are similar for both samples used in the spectroscopic studies: $L = 2.7 \pm 0.3$ nm ($Cu_{0.47}In_1S_y$ QDs) and $L = 2.8 \pm 0.4$ nm ($Cu_{0.85}In_1S_y$ QDs).

As expected on the basis of their similar mean size, both studied samples exhibit nearly identical bandgaps of ~2.25 eV as inferred from the spectral position of the minimum in the second derivative of the linear absorption spectrum, $\alpha(h\nu)$, typically used as an indicator of E_g in samples with weakly pronounced absorption features (inset of Figure 1b); here $h\nu$ is the photon energy presented as the product of the Planck constant (h) and the photon frequency (ν). Both QD samples exhibit a similarly large Stokes shift typical of CIS structures (420 and 340 meV for $x = 0.85$ and 0.47; respectively; Figure 1b,c) and long, hundreds-of-nanosecond PL lifetimes (Figure S2). They are also characterized by comparable PL quantum yields of 30% ($Cu_{0.85}In_1S_y$) and 28% ($Cu_{0.47}In_1S_y$). As demonstrated later in this work, despite apparent similarities in linear absorption and PL spectra, more sophisticated optical and magneto-optical techniques reveal considerable differences between these two samples, indicating a strong influence of sample stoichiometry on the photophysical properties of CIS QDs, which is likely linked to the relative abundance of Cu^{2+} *vs* Cu^{1+} defects.

Magnetic Circular Dichroism Measurements. In many semiconductor materials, MCD spectroscopy (see Methods and Experimental Section) can be used to detect and characterize the presence of paramagnetism and/or ferromagnetism that arises from the presence of magnetic dopants and impurities. In general, MCD detects the difference in the sample's absorption coefficient for right- and left-circularly polarized light ($\Delta\alpha_{MCD}$). When the band-edge states of a semiconductor are Zeeman-split by an applied magnetic field **B**, the resulting MCD spectrum typically follows the first derivative of the absorption spectrum. In nonmagnetic materials, the Zeeman splitting ΔE_Z, and therefore the MCD signal, is typically small, linear in **B**, and independent of temperature T. In contrast, when paramagnetic dopants exist in the material and further couple to the conduction and valence bands, ΔE_Z can be markedly enhanced and will follow the T-

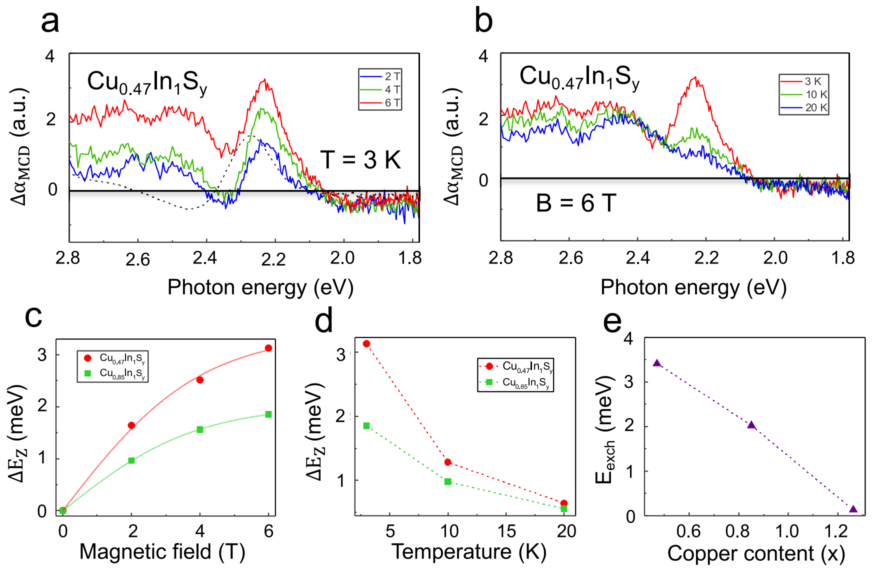

Figure 2. (a) MCD spectra of the *x* = 0.47 CIS QD sample as a function of magnetic field (B = 0−6 T) measured at *T* = 3 K (colored lines). The dashed black line is the first derivative of the absorption spectrum (α'); as expected, the overall shape of the α' spectrum is similar to that of the MCD spectra. (b) MCD spectra of the same sample as a function of temperature measured for B = 6 T. (c, d) The magnetic field and temperature dependence of the Zeeman splitting ΔE_Z obtained from data in panels a and b, respectively. (e). ΔE_{exch} as a function of copper content (*x*). The data point for the CIS QDs with *x* = 1.26 is from ref 41.

and **B**-dependent paramagnetic magnetization of the embedded dopants. In this case, the MCD signal will have a component (its paramagnetic part) that is strongly dependent on *T* and that saturates at large **B**.[10,47−49]

Here, we use MCD measurements to correlate the abundance of Cu^{2+} defects with the degree of Cu deficiency in our CIS QDs. The MCD technique is well suited for distinguishing between the 1+ and 2+ oxidation states of the Cu ion. Cu^{1+} (Cu_{In}'') ions have a filled $3d^{10}$ shell and are nonmagnetic, while Cu^{2+} ($Cu_{Cu}^{\bullet}$) ions are paramagnetic, spin-1/2 species because their $3d^9$ shell contains one unpaired spin. MCD studies have been previously used to detect signatures of paramagnetism in CIS QDs, which were attributed to the presence of Cu^{2+} defects.[41]

Figure 2a shows MCD spectra of the *x* = 0.47 sample recorded at *T* = 3 K for **B** from 0 to 6 T. Temperature-dependent MCD spectra for this sample measured at 6 T are shown in Figure 2b. The low-temperature absorption and PL spectra of the *x* = 0.47 sample along with spectroscopic data for the *x* = 0.85 sample can be found in Figure S3.

As expected, the shape of the MCD spectra of the CIS QDs is similar to that of the first derivative of the linear absorption spectrum ($\alpha'(h\nu)$; dashed black line in Figure 2a).[49] Applying a standard MCD analysis to these measurements,[48,49] we use the amplitude of the MCD peak to infer the Zeeman splitting, ΔE_Z, of the band-edge exciton. The derived values of ΔE_Z saturate at large **B** (Figure 2c) and, further, are strongly temperature dependent (Figure 2d). These observations unambiguously reveal the presence of paramagnetic species in the QDs whose spins are aligned by **B**, which in turn enhances the effective magnetic field experienced by the band-edge exciton. This enhancement is usually described in terms of spin exchange interactions between the paramagnetic impurities and intrinsic exciton states.[47] Its contribution to the total Zeeman splitting can be quantified as a product of the "exchange energy" (ΔE_{exch}) and the average spin projection of the paramagnetic species along **B** ($\langle S_Z \rangle$); the latter is usually described by a Brillouin-type dependence on *T* and **B**.[47]

For the *x* = 0.47 QDs, we obtain ΔE_{exch} = 3.4 meV. A similar analysis of the *x* = 0.85 sample (Figures S3 and 2c, green squares) yields a smaller value of the exchange energy of 2.0 meV. Together with our previous measurements of the copper-rich sample (ΔE_{exch} = 135 μeV for *x* = 1.26; ref 41), these results indicate a consistent trend; that is, a decrease in the copper content leads to an increase in exchange energy, which likely occurs due to the increased amount of paramagnetic species (Figure 2e). This is exactly the trend expected in the Cu^{1+}/Cu^{2+}-defect model according to which the increase in copper deficiency promotes the formation of paramagnetic Cu^{2+} defects that act as charge compensating species for Cu vacancies.[39,41] Spectroscopic studies described in the next three sections also support the conclusion that in stoichiometric (or near-stoichiometric) CIS QDs the prevailing defects are antisite Cu^{1+} ions (Cu_{In}''), while in the copper-deficient QDs the dominant defect is Cu^{2+} occurring as a positively charged $Cu_{Cu}^{\bullet}$ state.

Transient Absorption Measurements. Subtle distinctions between QD samples with different copper contents can be seen in linear absorption spectra of samples with *x* = 0.85 and 0.47; see Figure 1 (*T* = 300 K) and Figure S3 (*T* = 15 K). In particular, the absorption edge of the near stoichiometric QDs with *x* = 0.85 is clearly broader than that of the Cu-deficient QDs and shows a greater absorptivity in the intragap region if $\alpha(h\nu)$ is normalized at the position of the nominal bandgap (see the inset of Figure 1c). A Cu-rich sample with *x* = 1.12 also shows a low-energy tail extending into the intragap region (Figure S4).

Since the samples with *x* = 0.85 and 0.47 are characterized by similar size dispersions, the smearing of the absorption edge in the nearly stoichiometric sample cannot be explained by inhomogeneous broadening but rather indicates an increased contribution from lower-energy intraband transitions. This effect, in particular, is consistent for the situation of the

https://dx.doi.org/10.1021/acsnano.9b09181
ACS Nano 2020, 14, 2212−2223

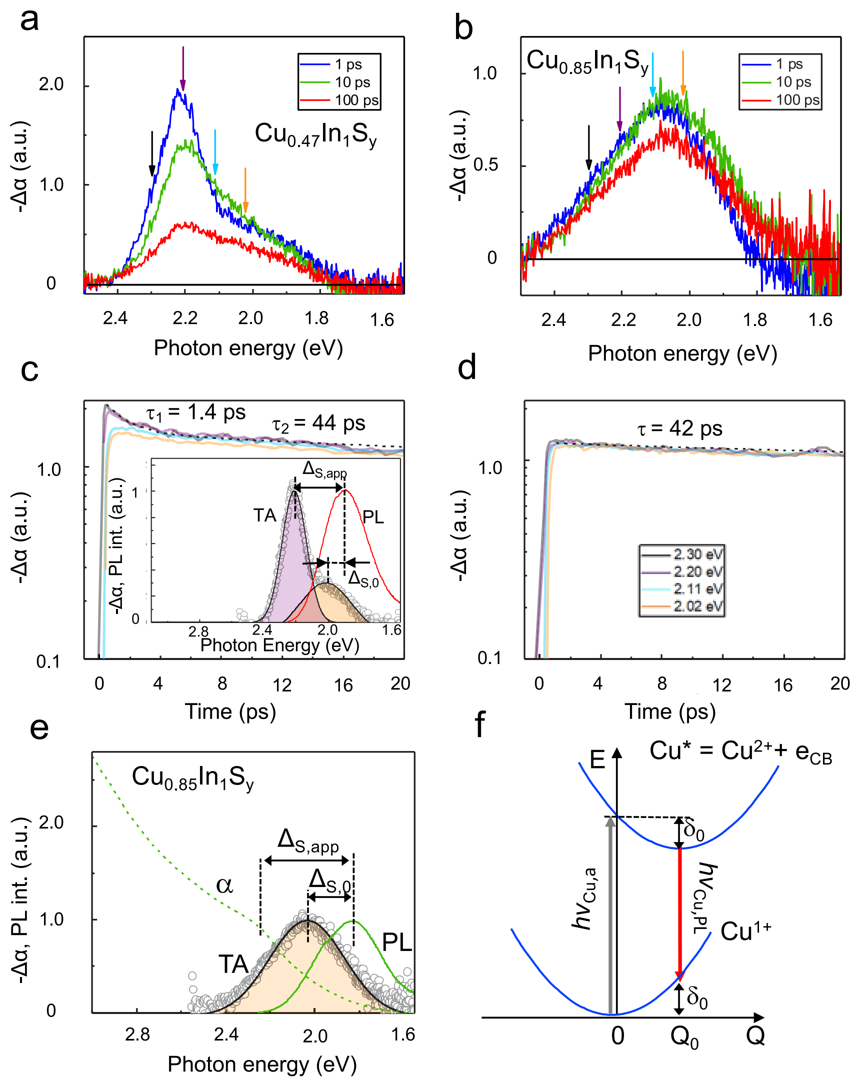

Figure 3. (a, b) TA spectra of the CIS QDs with $x = 0.47$ (a) and $x = 0.85$ (b) measured for pump−probe delay times $\Delta t = 1$, 10, and 100 ps using femtosecond (<190 fs), 3.61 eV pump pulses. These measurements were conducted using low, subsingle-exciton pump fluences when the average number of electron−hole pairs generated per-dot, per-pulse ($\langle N\rangle$) was much less than 1. (c, d) Spectrally resolved TA dynamics for the $x = 0.47$ (c) and 0.85 (d) samples measured using probe photon energies shown by color-matched arrows in (a) and (b), respectively. Inset in (c): The early time TA spectrum ($\Delta t = 1$ ps) of the $x = 0.47$ sample (gray circles) can be presented as a superposition of the band-edge bleach (VB−CB transition; purple shading) and the Cu^{1+} bleach (Cu^{1+}−CB transition; orange shading). The shifts of these bleach features *vs* the PL band (red line) define, respectively, the apparent ($\Delta_{S,app}$) and the true ($\Delta_{S,0}$) Stokes shifts. (e) The apparent and the true Stokes shifts in the case of the $x = 0.85$ sample. Since in this case the band-edge bleach is not pronounced in the TA spectra, the position of the VB−CB transition is determined from the analysis of the second-derivative (α'') of the absorption spectrum (α is shown by the dashed green line). (f) A displaced-harmonic oscillator model, which explains the development of the true Stokes shift in the case of the Cu^{1+} defect. The bottom parabola represents the dependence of the ground-state energy of the coupled QD-Cu-defect system on configuration coordinate Q, which can be thought of as a quantity describing the relative position of the Cu defect within the crystal lattice of the QD. The top parabola is the excited state of this system composed of a photogenerated CB electron and an excited Cu^{2+} like state formed *via* localization of a photogenerated VB hole on the Cu^{1+} defect. The minimum of the top parabola is displaced *vs* Q = 0 due to the reorganization of the crystal lattice around the Cu defect following its excitation. The energies of vertical absorbing (gray line) and emitting (red line) transitions are different by twice the vibrational relaxation energy (δ_0), which defines the true Stokes shift: $\Delta_{S,0} = 2\delta_0$.

increased abundance of Cu^{1+} defects. As we discussed earlier, these defects are "absorption active" and are optically coupled to the CB states, which produces optical absorption below the bandgap ($h\nu_{Cu,a}$ in Figure 1a, left). A similar trend, that is, progressive broadening (smearing) of the band-edge feature with increasing x, was observed in ref 4, where it was also ascribed to the increasing intensity of the intraband Cu^{1+}−CB transition accompanying the increase in the Cu-to-In ratio.

While the distinctions between linear absorption spectra of samples with different degrees of Cu deficiency can be comparable to those due to batch-to-batch variability, the corresponding distinctions between TA spectra are considerably more pronounced. In the TA experiment, we apply a pump−probe spectroscopy for monitoring time and spectrally resolved changes in the absorption spectrum ($\Delta\alpha$) of a QD sample induced by a short pump pulse (<190 fs duration) with a 3.61 eV photon energy; see the Methods and Experimental Section for details of the TA measurements. In Figure 3a,b, we display a series of TA spectra of samples with $x = 0.47$ and 0.85, respectively, measured for pump−probe delays (Δt) from

1 to 100 ps using low excitation levels when the average number of excitons generated per pulse per dot, $\langle N \rangle$, is less than 0.1, which allows us to avoid complications due to multiexciton effects.

The early time TA spectra (Δt = 1 and 10 ps) of the more Cu-deficient sample exhibit a band-edge bleach with a clear two-band structure. On the basis of a double-Gaussian fit (inset of Figure 3c), the higher-energy peak is located at $h\nu_{\mathrm{TA},1}$ = 2.21 eV, which is near the sample bandgap inferred from the analysis of the second derivative of the absorption spectrum (inset of Figure 1b). The lower-energy feature is at $h\nu_{\mathrm{TA},2}$ = 2.02 eV, which corresponds to the intragap region. We ascribe these two TA bands to, respectively, the intrinsic VB−CB excitonic transition ($h\nu_{\mathrm{TA},1} = h\nu_{x,\mathrm{a}}$) and the Cu-defect-to-CB transition ($h\nu_{\mathrm{TA},2} = h\nu_{\mathrm{Cu,a}}$); see Figure 1a. A strong difference in dynamics of the two bands (Figure 3c) is consistent with this assignment. Indeed, on the basis of the present study as well as a large body of existing literature,[7−9,12,39−42,44] CIS QDs never exhibit a band-edge PL, suggesting that the intrinsic excitons are short-lived. In samples with the prevailing Cu^{1+} defects, exciton decay likely occurs *via* hole trapping at negatively charged $\mathrm{Cu_{In}}''$ sites. In the case of the Cu^{2+} defects, the VB holes can be quickly removed due to trapping at the charge compensating negatively charged copper vacancies (V_{Cu}'). The observed very short lifetime of the higher-energy TA feature (τ_1 = 1.4 ps, Figure 3c) is consistent with the fast decay of the band-edge exciton due to the quick removal of a photogenerated hole from the VB state. On the basis of the resonant PL and PLE studies discussed later in this work, our samples can be thought of as being composed of two QD subensembles with distinct emission channels mediated by either Cu^{1+} or Cu^{2+} defects. In TA measurements, these two subensembles are expected to exhibit two different time scales of VB hole relaxation. One of them is defined by hole trapping at the Cu^{1+} centers (subensemble with the Cu^{1+} emission path), while the other, by hole trapping at some other unoccupied intragap states (subensemble with the Cu^{2+} emission path); as suggested earlier, these states are likely Cu vacancies that are expected to accompany the Cu^{2+} defects for charge compensation. The measured initial TA decay constant (τ_1 = 1.4 ps) likely describes the fastest of these processes.

As expected, the lower-energy TA band ($h\nu_{\mathrm{TA},2}$), attributed to the intragap Cu-defect-related transition, is considerably longer lived than the intrinsic band-edge feature as its dynamics is governed by the relaxation of the CB electron. In well passivated samples, it is controlled by a long radiative lifetime of the intragap transition (hundreds of nanoseconds).[7−12,39−42,44] In samples with imperfect passivation, its relaxation is due to fairly slow electron surface trapping,[8,39,44] which is likely observed here as a slower TA decay characterized by τ_2 = 44 ps (Figure 3c).

The above two-band model of the band-edge TA is supported by the measurements of QDs with x = 0.85. Compared to the strongly Cu-deficient sample, in this nearly stoichiometric sample, we expect an increased abundance of "absorption-active" Cu^{1+} defects. As discussed earlier, the increased per-dot number of Cu^{1+} defects is likely responsible for the extended low-energy tail in the linear absorption (inset of Figure 1c). This is also anticipated to lead to the relative increase of the intragap $h\nu_{\mathrm{TA},2}$ TA feature *vs* the band-edge $h\nu_{\mathrm{TA},1}$ band compared to the Cu-deficient QDs. This expected spectral redistribution of the TA signal in favor of the $h\nu_{\mathrm{TA},2}$ band is observed experimentally. Indeed, the measured TA spectra of the x = 0.85 sample is dominated by the lower-energy ∼2.0 eV band (Figure 3b) whose dynamics (τ = 42 ps; Figure 3d) are similar to that of the slower decay observed for the x = 0.47 sample. The higher-energy $h\nu_{\mathrm{TA},1}$ bleach in this case manifests only as a weak, short-lived "blue" tail of the main intragap TA feature. A similar situation, that is, the dominance of the intragap ($h\nu_{\mathrm{TA},2}$) TA band, is also realized in the Cu-rich sample with x = 1.12 (Figure S4).

The analogous two-band model was previously utilized in ref 4 to rationalize spectral modifications in the TA spectra occurring as a result of changes in the Cu-to-In ratio. In particular, the authors of that study also observed the increase in the relative amplitude of the higher-energy ($h\nu_{\mathrm{TA},1}$) TA band *vs* the lower-energy ($h\nu_{\mathrm{TA},2}$) feature with an increasing degree of Cu deficiency.

Interestingly, the spectral energy of the intragap TA band for the x = 0.47 sample ($h\nu_{\mathrm{TA},2} = h\nu_{\mathrm{Cu,a}} \approx 2.04$ eV) is distinct from that of the intragap PL ($h\nu_{\mathrm{Cu,PL}} \approx 1.83$ eV; Figure 3e), while they both are nominally due to the same optical transition, which couples the Cu defect to the QD CB state. The difference between energies $h\nu_{\mathrm{Cu,a}}$ and $h\nu_{\mathrm{Cu,PL}}$ arises from reorganization of lattice ions around the Cu defect upon its excitation, which can be understood using a displaced harmonic oscillator model depicted in Figure 3f. This model presents the total energy of a solid-state system as a sum of the energy of electronic motion and that of nuclei vibrations of a crystal lattice. The potential energy of lattice vibrations is usually approximated by a quadratic (parabolic) function of a configuration coordinate (Q), which describes the arrangement of lattice nuclei. Due to interactions between electronic and lattice degrees of freedom, the configuration coordinate, which corresponds to the state of equilibrium of the coupled electron−lattice system (Q_{eq}; defined by the minimum of the parabola), changes upon excitation of the electronic subsystem.

In the scheme of Figure 3f, we apply the displaced harmonic oscillator representation to describe the absorption−emission cycle for a Cu^{1+} defect. Here, we assume $Q_{\mathrm{eq}} = 0$ in the unexcited Cu^{1+} state (the lower parabola in Figure 3f). When the Cu ion is excited to the Cu^{2+}-like state by promoting its 3d electron into the QD CB, Q_{eq} changes from 0 to Q_0. This excited copper state (Cu*) corresponds to the upper parabola in Figure 3f where it is denoted as $\mathrm{Cu}^* = \mathrm{Cu}^{2+} + e_{\mathrm{CB}}$. According to the Franck−Condon principle, optical transitions are vertical in the Q-space (*i.e.*, occur without changes in nuclei coordinates). As a result, the formation of the Cu* state is accompanied by the excitation of lattice vibrations with energy δ_0 (Figure 3f). Following fast vibrational relaxation, the Cu* state "cools down" to the bottom of the parabola and then experiences a radiative transition back to the Cu^{1+} state. However, as stated earlier due to the vertical nature of the optical transition, this is also accompanied by generating vibrational energy δ_0. These considerations indicate that the energies of the absorbing ($h\nu_{\mathrm{Cu,a}}$) and the emitting ($h\nu_{\mathrm{Cu,PL}}$) transitions are different by twice the vibrational energy: $h\nu_{\mathrm{Cu,PL}} = h\nu_{\mathrm{Cu,a}} - 2\delta_0$ (Figure 3f). The value $\Delta_{\mathrm{S},0} = 2\delta_0$ constitutes a true Stokes shift, which is the difference between absorption and emission energies involving transitions between the *same* electronic states (in this case, the unexcited and excited states of the Cu^{1+} ion). This true Stokes shift is distinct from the apparent Stokes shift ($\Delta_{\mathrm{S,app}}$) defined by the energy difference between the absorption feature due to the intrinsic QD VB-to-CB transition ($h\nu_{x,\mathrm{a}}$) and the intragap emission due to radiative

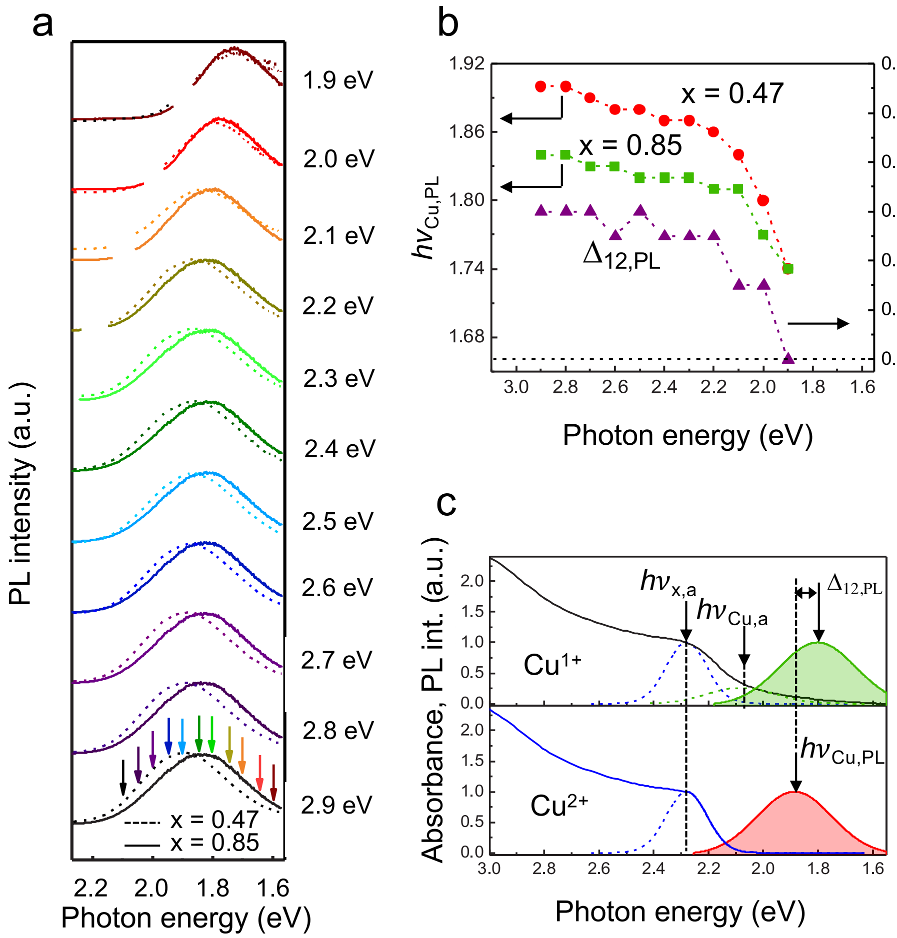

Figure 4. (a) Resonant PL measurements of the CIS QD samples with x = 0.85 (solid lines) and 0.47 (dashed lines) using near-band-edge excitation with photon energy ($h\nu_p$) tuned from 2.9 to 1.9 eV in 0.1 eV increments. (b) The PL peak energies for samples with x = 0.85 (green squares) and 0.47 (red circles) along with their difference ($\Delta_{12,PL}$; purple triangles) as a function of $h\nu_p$. (c) Simulated absorption (solid lines) and emission (colored shading) spectra of CIS QDs in the presence of Cu^{1+} (top) and Cu^{2+} (bottom) defects. In the former case, the absorption edge comprises features due to both the intrinsic CB−VB transition (blue dashed line) and the intragap Cu^{1+}−CB transition (green dashed line). In the latter case, the absorption edge is entirely due to the CB−VB transition as the Cu^{2+} defects are nonabsorbing. The energies of PL due to Cu^{1+} and Cu^{2+} defects are distinct because of the different lattice environments of $\mathrm{Cu_{In}}''$ and $\mathrm{Cu_{Cu}}^{\bullet}$ centers. The measured resonant PL spectra can be explained by assuming that our samples consist of two QD subensembles, one of which contains dots with the Cu^{1+} defects and the other comprises dots with the Cu^{2+} defects. Because the Cu^{1+} defects absorb in the intragap region, while the Cu^{2+} defects do not, the emission from the former ensemble becomes selectively enhanced when the excitation energy shifts below the energy of the intrinsic VB−CB transition. This leads to the lower-energy shift of the overall PL spectrum observed experimentally.

relaxation of the Cu* state ($h\nu_{Cu,PL}$). The true and the apparent Stokes shifts are connected by the expression $\Delta_{S,app} = \Delta_{S,0} + \Delta_{Cu}$, where $\Delta_{Cu} = h\nu_{x,a} - h\nu_{Cu,a}$. On the basis of the TA spectrum of the nearly stoichiometric sample (x = 0.85), wherein the prevailing PL mechanism is Cu^{1+} emission, $h\nu_{Cu,a}$ = 2.04 eV (Figure 3b,e). The PL of this sample is centered at $h\nu_{Cu,PL}$ = 1.83 eV (Figure 1b). These values yield $\Delta_{S,0} = h\nu_{Cu,a} - h\nu_{Cu,PL}$ = 210 meV (Figure 3e). On the basis of the measured PL energy and the bandgap of 2.25 eV, $\Delta_{S,app}$ = 420 meV. Thus, Δ_{Cu} = 210 meV. This value represents the energy difference between the intrinsic QD band-edge transition and the Cu^{1+} "absorbing" transition.

In the above analysis, we considered direct excitation of the Cu ion by a photon with an intragap energy. Commonly, however, QDs are excited *via* the VB−CB transition using photons with the above bandgap energy. In this case, the excitation of a Cu^{1+} ion occurs by trapping a VB hole. Observation of emission from the excited Cu^{1+} state also requires a CB electron. Therefore, the excited emissive state of the Cu^{1+} ion (Cu*) can be viewed as an exciton localized on the negatively charged $\mathrm{Cu_{In}}''$ defect. This situation is somewhat similar to that in the model of a self-trapped exciton.[10,11] In both models, the electron resides in the intrinsic band-edge state delocalized across the entire QD, while the hole is confined to a single Cu ion. In both cases, the strong carrier-phonon coupling, typical of localized states, leads to the large Stokes shift of the emission band *vs* the absorption feature, which can be described by the displaced harmonic oscillator model (Figure 3f). The distinction between the two models is that, in the case of the self-trapped exciton, the hole is localized on the "correct" Cu site of the defect-free crystal lattice, while in the Cu^{1+}-defect model, the excitation resides on the "wrong" (In) lattice site ($\mathrm{Cu_{In}}''$).

While either model can, in principle, explain the development of intragap emission, the self-trapped exciton model still needs to bridge the nanoscale and bulk regimes and, in particular, rationalize why exciton self-localization does not occur in macroscopic CIS crystals.[10,11] A related challenge is to provide an explanation to observations in which, even in very large CIS QDs with the absorption onset near the bulk CIS bandgap ($E_{\mathrm{g,bulk}}$ = 1.52 eV), the emission is still strongly Stokes shifted and extends well below $E_{\mathrm{g,bulk}}$.[40,50] These observations are difficult to rationalize in terms of exciton self-trapping as its influence should greatly diminish at large (bulk-like) QD sizes. Therefore, here, we assume that the lower-energy emission channel prevailing in stoichiometric and Cu-rich samples is associated with the $\mathrm{Cu_{In}}''$ defect. It complements the intragap absorption process arising from the Cu^{1+}−CB transition.

As we discussed earlier in this work, the mechanism of activation of emission from a Cu^{2+} defect is distinct from that for a Cu^{1+} defect. Since the 3d shell of the Cu^{2+} ion contains a hole-like vacancy, this defect is immediately "emission-ready". Therefore, if a photoexcited hole is promptly removed from the VB state (due to trapping by, *e.g.*, a Cu vacancy), the Cu^{2+} defect can radiatively trap the CB electron, which leads to intragap emission. While from the "electronic perspective" an excited Cu^{1+} state is analogous to the Cu^{2+} defect, these two states can have different total energies due to distinct lattice environments. The Cu^{1+} defect occurs on the In^{3+} site of an ideal (defect-free) CIS lattice ($\mathrm{Cu_{In}}''$). On the other hand, the Cu^{2+} defect is located on its copper site ($\mathrm{Cu_{Cu}}^{\bullet}$). As a result, the vibrational frequency (*i.e.*, the curvature of parabolas in Figure 3f), the equilibrium configuration coordinate (Q_0), and the lattice relaxation energy (δ_0) can be different between the two states. This would lead to different Stokes shifts (both true and apparent) and, as a result, different emission energies even when the QD bandgap is the same in both cases.

The difference in emission energies and $\Delta_{\mathrm{S,app}}$ between a nearly stoichiometric (x = 0.85) and a copper-deficient (x = 0.47) sample is evident from the absorption and PL measurements displayed in Figure 3e and the inset of Figure 3c. On the basis of the measured spectra, $h\nu_{\mathrm{Cu,PL}}$ is 1.83 and 1.91 eV for x = 0.85 and 0.47, respectively. The corresponding apparent Stokes shifts are 420 and 340 meV. As discussed in the next two sections, resonant PL and PLE measurements further confirm the existence of two distinct emission and absorption mechanisms associated with two different types of Cu defects (Cu^{1+} and Cu^{2+}). In fact, as we show below, these two mechanisms can coexist in the same QD ensemble and their relative contributions depend on sample stoichiometry, which defines the relative fraction of QDs with predominantly Cu^{1+} *vs* Cu^{2+} emission.

Resonant PL Measurements. In the resonant-PL experiment, we monitor PL spectra as a function of pump photon energy ($h\nu_{\mathrm{p}}$) tuned from above to below the QD bandgap (2.9 to 1.9 eV) with a 0.1 eV increment. In Figure 4a, we display the results of these measurements for $\mathrm{Cu_{0.85}In_1S}_y$ and $\mathrm{Cu_{0.47}In_1S}_y$ QD samples (solid and dashed lines, respectively). The $h\nu_{\mathrm{p}}$-dependent PL peak energies ($h\nu_{\mathrm{Cu,PL}}$) and the spacing between them, $\Delta_{12,\mathrm{PL}} = h\nu_{\mathrm{Cu,PL}}$ (x = 0.47) − $h\nu_{\mathrm{Cu,PL}}$ (x = 0.85), are plotted as a function of $h\nu_{\mathrm{p}}$ in Figure 4b.

The collected data indicates that, when the pump photon energy is above or near the bandgap ($h\nu_{\mathrm{p}} \geq 2.2$ eV), the PL peak moves only slightly to lower energies with decreasing $h\nu_{\mathrm{p}}$. The spectral shifts are similar for both samples; therefore, the emission energy of the QDs with x = 0.47 remains higher than that of the x = 0.85 sample by a nearly constant value of 50−70 meV. This behavior can be ascribed to the effect of "spectroscopic size selection", which occurs due to excitation of progressively lager particles with a smaller bandgap from a polydisperse QD ensemble.[51] In the case of CIS QDs, however, this effect is weak as the PL ensemble line width is dominated not by QD size dispersion but by the distribution of the Cu-defect energies;[42,43] hence, the observed spectral shifts are small.

The spectral modifications become more dramatic in the range of lower excitation energies. In particular, as $h\nu_{\mathrm{p}}$ moves past 2.2−2.1 eV, the low-energy shift of the PL peak sharply accelerates (Figure 4b). For the QDs with x = 0.85, the shift occurs faster than for the x = 0.47 sample, so eventually, both spectra merge together and become virtually indistinguishable when $h\nu_{\mathrm{p}}$ reaches 1.9 eV.

The above observations support our early suggestion of spectrally distinct emission bands associated with the Cu^{2+} and Cu^{1+} defects (Figure 4c). For the above-E_{g} excitation energies, the Cu^{2+} and Cu^{1+} emission channels are both operative due to activation through the QD host, which serves as a light-absorbing mediator. As a result, the observed PL is a combination of two closely spaced bands associated with the two channels. The PL spectrum, however, is biased to either lower or higher energies depending on the degree of Cu deficiency. In a strongly Cu-deficient sample with x = 0.47, the PL spectrum is shifted to higher energies due to the increased weight of the Cu^{2+} emission pathway (Figure 4c, bottom panel). On the other hand, in the nearly stoichiometric sample (x = 0.85), emission is dominated by Cu^{1+} defects and, therefore, the PL band moves toward lower energies (Figure 4c, top panel). In a given sample, however, the branching between the two emission pathways is independent of $h\nu_{\mathrm{p}}$, as both are activated through the same host particle. As a result, the changes in the spectral position of the PL peak are small as long as $h\nu_{\mathrm{p}}$ is greater than the bandgap.

The situation, however, changes in the sub-bandgap region. When $h\nu_{\mathrm{p}}$ shifts below E_{g}, QD excitation *via* intrinsic VB-to-CB transitions becomes less effective, while the role of direct excitation of Cu defects increases. Since Cu^{2+} states are nonabsorbing, sub-bandgap excitation preferentially activates the Cu^{1+} defects. This is expected to enhance the contribution from the Cu^{1+} emission channel (lower transition energy) and simultaneously suppress Cu^{2+} emission (higher transition energy). This explains a rapid low-energy shift of the PL spectrum in the range of $h\nu_{\mathrm{p}} < \sim 2.1$ eV due to its gradual conversion into the pure Cu^{1+} emission band observed for both samples (Figure 4a,b).

PLE Measurements. The PLE studies provide further evidence for the existence of two distinct Cu^{1+} and Cu^{2+} emission bands. In the PLE measurements, we monitor the PL signal at several fixed detection energies within the PL band ($h\nu_{\mathrm{det}}$ = 2.1 to 1.6 eV) while continuously tuning $h\nu_{\mathrm{p}}$ from 2.9 to 1.9 eV. In our model of spectrally separated PL bands of Cu^{1+} and Cu^{2+} defects, we expect to isolate their absorption signatures by tuning the detection energy to, respectively, lower- and higher-energy parts of the overall emission spectrum (Figure S5). In the former case, we will preferentially probe the Cu^{1+} emission channel, and hence, the measured PLE spectrum should comprise absorption features due to both the QD host and the absorbing Cu^{1+} defect. In the latter case, the PLE is expected to be almost exclusively due to intrinsic QD transitions as the Cu^{2+} defects are nonabsorbing.

The above trends are clearly observed in the case of the nearly stoichiometric x = 0.85 sample (Figure 5a). When the detection energy is on the higher-energy side of the PL band

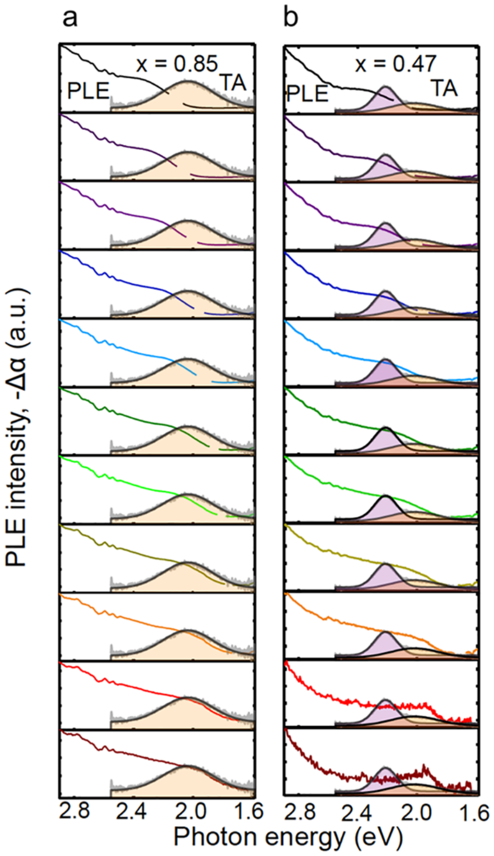

Figure 5. (a) PLE measurements of the CIS QDs with x = 0.85 conducted by monitoring the PL signal at a fixed spectral energy ($h\nu_{det}$) within the PL profile while continuously tuning the pump photon energy from 2.9 to 1.9 eV. The PLE spectra shown in this panel were obtained using 11 detection energies varied from 2.1 (top) to 1.6 eV (bottom). The specific detection energies are shown by color-matched arrows at the bottom of Figure 4a. (b) Similar measurements conducted for the sample with x = 0.47. The $h\nu_{det}$-dependent evolution of the PLE spectra can be understood using the model of two QD subensembles with distinct emission and absorption spectra as schematically depicted in Figure 4c. In particular, when the PLE data are acquired using $h\nu_{det}$ tuned to a high-energy side of the PL spectrum, this leads to preferential selection of the Cu^{2+} QD subensemble, which is characterized by a higher emission energy compared to the subensemble with the Cu^{1+} defects. As a result, the measured PLE exhibits a fairly sharp onset near E_g without a considerable contribution from the intragap Cu^{1+}-related absorption. On the other hand, when the PL is monitored on the lower-energy side of the emission profile, the PLE measurement emphasizes the Cu^{1+}-subensemble, which leads to an enhancement of the signal in the intraband region due to the relative increase of the Cu^{1+}−CB absorption feature. Indeed, the comparison of the PLE and TA spectra at the bottom of the panel indicates that the onset of the growth of the intragap PLE signal occurs when $h\nu_p$ shifts below the intersection of the band-edge and Cu^{1+}-related TA features, that is, when $h\nu_p$ enters the spectral region where sample absorption is dominated by direct excitation of the Cu^{1+} ion.

($h\nu_{det}$ > 1.9 eV), the measured PLE spectrum exhibits a fairly sharp onset near the energy of the intrinsic band-edge exciton ($h\nu_{x,a}$). However, when the detection energy shifts to lower energies past the PL peak ($h\nu_{det}$ < 1.9 eV), the PLE spectrum develops an intragap tail, which matches the TA feature due to the absorbing Cu^{1+} transition (shaded spectrum in Figure 5a).

The intragap absorption is even more pronounced in the PLE measurements of the copper-deficient x = 0.47 sample (Figures 5b and S5). For higher detection energies ($h\nu_{det}$ > 1.9 eV), the observed PLE spectrum is dominated by intrinsic absorption due to the semiconductor host, as in the case of the x = 0.85 sample. In fact, the absorption edge revealed by the PLE measurements closely matches the excitonic band-edge feature observed in an early time TA spectrum (Figure 3d, the band shown by purple shading). The trends detected in the range of lower probe energies ($h\nu_{det}$ < 1.9) are slightly different from those displayed by the x = 0.85 sample. In particular, as $h\nu_{det}$ moves to the red side of the PL peak, the PLE signal exhibits the expected growth of an intraband feature in the spectral region of the Cu^{1+}−CB absorbing transition revealed by TA measurements (Figure 3c, orange shading). Eventually, however, the PLE signal due to defect-related absorption becomes more intense than that due to QD intrinsic band-edge absorption. This suppression of the intrinsic excitonic contribution in the PLE spectrum is not observed for the x = 0.85 sample, which provides additional evidence for the dominant role of Cu^{2+} defects in the copper-deficient QDs. Indeed, when the Cu^{2+} defects prevail over the Cu^{1+} defects, the majority of excitons generated *via* the VB−CB transitions recombine through the Cu^{2+} emission channel. However, due to its higher emission energy, this channel does not contribute to the PLE measured on the red side of the PL band since it is dominated by the lower-energy emission from the Cu^{1+} defects. This explains the relative enhancement of the intraband Cu^{1+} related PLE feature *vs* intrinsic band-edge absorption in copper deficient QDs when they are probed on the red side of the PL band.

CONCLUSIONS

We have conducted comprehensive studies of $Cu_xIn_1S_y$ QD samples with varied degrees of Cu deficiency using linear absorption, PL (resonant and nonresonant), and PLE spectroscopies as well as femtosecond TA and magneto-optical MCD measurements. These studies reveal clear distinctions between samples with different Cu-to-In ratios, which can be ascribed to the difference in relative abundance of Cu^{2+} *vs* Cu^{1+} defects. In particular, as indicated by MCD studies, the increase in copper deficiency leads to an increased strength of the paramagnetic component of the MCD signal, which we attribute to the increasing amount of paramagnetic spin-1/2 Cu^{2+} defects. We observe that ensemble QD samples emit simultaneously *via* both Cu^{2+} *vs* Cu^{1+} channels that are characterized by slightly different emission energies revealed by resonant PL and PLE measurements. These measurements along with the TA studies also clarify stoichiometry-dependent mechanisms for light absorption in CIS QDs. In particular, a large abundance of Cu^{1+} defects in nearly stoichiometric samples increases the strength of intragap absorption due to the Cu^{1+}-to-CB transitions, which manifests as an extended sub-bandgap absorption tail. On the other hand, the increase in the degree of copper deficiency, which promotes nonabsorbing Cu^{2+} defects, suppresses intragap absorption and leads to an apparent sharpening of the absorption edge.

The conducted measurements also suggest the existence of two types of a Stokes shift: true and apparent. The true Stokes shift ($\Delta_{S,0}$) characterizes the displacement between the energy of the defect-related emission and the energy of Cu^{1+} absorption due to the reorganization of lattice atoms around the excited-state defect site. Because of a localized character of such reorganization, $\Delta_{S,0}$ is not QD size dependent but is defined solely by the strength of carrier-phonon coupling. On the other hand, the apparent Stokes shift ($\Delta_{S,app}$), which represents the spectral separation between the intrinsic (VB−CB) QD band-edge absorption and the defect-related emission, is contributed to by both the energy of carrier−phonon interactions and carrier confinement. Therefore, if required, $\Delta_{S,app}$ can be tuned by changing the QD size.

The insights gained from the conducted studies have important implications for CISeS QD applications in sunlight harvesting technologies including, in particular, LSCs[23−27,52] and QD-sensitized photovoltaics (PVs).[1,16−19] A critical performance-limiting factor of LSCs is self-absorption by the QDs during light propagation in the LSC waveguide. Given the results of the present study, the effects of self-absorption can, in principle, be reduced by using Cu-deficient samples wherein the intragap Cu^{1+} related absorption is suppressed. Importantly, the use of Cu-deficient samples will likely not lead to diminishing PL, as on the basis of our present study, the PL quantum yields of strongly Cu-deficient QDs (28% for x = 0.47) are comparable to those of nearly stoichiometric samples (30% for x = 0.85).

The opposite situation, that is, the dominance of Cu^{1+} defects, is likely beneficial to PV devices utilizing CISeS QDs, as it should allow one to extend sample absorbance into the intragap region and thereby enhance light harvesting and, consequently, short-circuit current (J_{sc}). Normally, the development of an intragap tail in the density of states is undesirable for PV materials, as it leads to the reduction of the open-circuit voltage (V_{oc}). In the case of the CISeS QDs, however, V_{oc} is always "pinned" by the energy of the Cu^{1+}−CB transition due to fast trapping of the VB hole (see our earlier discussion). Therefore, activation of intragap Cu^{1+} defect-related absorption should enhance J_{sc} without detrimentally affecting V_{oc}.

The overall conclusion of our study is that the band-edge optical properties of CIS QD samples are strongly influenced by native optically active Cu defects that seem to be unavoidable at least for the existing chemical synthesis approaches. These defects occur as both Cu^{1+} and Cu^{2+} species, and their relative abundance can be controlled during synthesis by tuning the degree of Cu deficiency. Along with traditional approaches exploiting the quantum size effect, the control of defect states provides an additional knob for tuning CIS(Se) QD electronic and optical properties and thereby realizing functionalities not accessible with structurally perfect materials.

METHODS AND EXPERIMENTAL SECTION

Chemicals and Materials. The following chemicals were purchased and used as received. Anhydrous copper(I) iodide (CuI, 99.995%), 1-dodecanethiol ($CH_3(CH_2)_{11}SH$, DDT, ≥98%), anhydrous chloroform (CH_3Cl, ≥99%), and anhydrous methanol (CH_3OH, ≥99%) were obtained from Sigma-Aldrich. Anhydrous indium(III) acetate ($In(CH_3COO)_3$, $In(Ac)_3$, 99.99%) and oleylamine ($CH_3(CH_2)_7CH{=}CH(CH_2)_7CH_2NH_2$, OLAm, 80−90%) were purchased from Acros Organics.

Synthesis of $Cu_xIn_1S_y$ Quantum Dots. Typically, x' mmol of CuI and 1 mmol of $In(Ac)_3$ were dissolved in 5 mL of DDT and 1 mL of OLAm in a 50 mL round-bottom flask, and the mixture was degassed under vacuum at 100 °C for 30 min. The temperature of the reactant mixture was raised to 140 °C until all solid precursors were fully dissolved, which usually took less than 10 min. For nucleation and growth, the temperature was set to 230 °C for 20 min. The heating element was then removed, and the QDs were allowed to cool. The resulting quantum dots (QDs) were purified by several cycles of dissolution in chloroform and precipitation with methanol and then stored in chloroform under an N_2 atmosphere. The actual content of copper (x) *vs* In in the synthesized QDs was determined using ICP-AES. Typically, it was higher than the nominal Cu content (x') based on the molar amounts of Cu and In precursors used in the reaction. Specifically, the use of x' = 1, 0.5, and 0.25 resulted in QDs with x = 1.12, 0.85, and 0.47, respectively.

Preparation of Quantum Dot Films. A QD solution (4 mL in chloroform) was added to a 5 mL solution of 2% w/w polyvinylpyrrolidone (PVP) in chloroform. After vigorous stirring, the mixture was transferred to a centrifuge tube, and then, the QDs were precipitated by adding hexane. After centrifuging with 5000 rpm for 5 min, the supernatant was discarded. The precipitated pellet was dissolved in 600 μL of 1% w/w butanol/chloroform solution to prepare a QD/polymer solution. The film was made by dropping the QDs/polymer solution onto a 5 mm-by-5 mm fused silica slide followed by spin coating with 500 rpm for 2 min and then 2000 rpm for 1 min.

Optical Spectroscopy Measurement. Optical absorption, photoluminescence (PL), PL excitation (PLE), and transient absorption (TA) measurements were conducted on QD/chloroform solutions. The PL and PLE were recorded using a Horiba Scientific Fluoromax-4 spectrometer. Absorption spectra were measured with an Agilent 8543 UV−visible spectroscopy system. TA measurements were conducted using a home-built pump−probe system. QD samples were excited using a frequency tripled (3.61 eV) output of a Pharos amplified Yb:KGW laser (<190 fs pulse duration), and the excited sample spot (200 μm diameter) was probed using variably delayed pulses of a broad-band white-light continuum probe. The white light was generated by focusing the laser beam at the fundamental frequency onto a sapphire plate (2 mm thickness). TA studies were conducted using low pump fluences ($<6 \times 10^{13}$ photons/cm^2) for which an average number of electron−hole pairs generated per dot per pulse $\langle N \rangle$ was less than 0.1. To avoid the effects of uncontrolled photocharging, the QD solution samples were vigorously stirred during the measurements.

Magnetic Circular Dichroism (MCD) Measurements. We used well-established methods for MCD spectroscopy[48,49] to measure the magnetic-field-induced Zeeman splitting of the absorption edge in our QD films. MCD measures the normalized difference in transmission between right- and left-circularly polarized light in the Faraday geometry. Strongly temperature-dependent MCD signals and/or the presence of enhanced MCD signals that saturate at high magnetic fields and low temperatures point to the presence of additional paramagnetic ions in the QDs. The QD films were mounted in a variable-temperature insert (T = 1.5−300 K) of a 7 T superconducting magnet with direct optical access. Wavelength-tunable probe light was derived from a Xe lamp directed through a 300 mm spectrometer. The probe light was mechanically chopped at 137 Hz and modulated between left- and right-circular polarization at 50 kHz using a photoelastic modulator. The transmitted light was detected with a silicon avalanche photodiode, and lock-in amplifiers were used to extract the MCD signal.

ASSOCIATED CONTENT

Supporting Information

The Supporting Information is available free of charge at https://pubs.acs.org/doi/10.1021/acsnano.9b09181.

Transmission electron microscopy images and additional linear absorption, transient absorption, photoluminescence, and magnetic circular dichroism measurements (PDF)

AUTHOR INFORMATION

Corresponding Author

Victor I. Klimov − *Los Alamos National Laboratory, Los Alamos, New Mexico;* orcid.org/0000-0003-1158-3179; Email: klimov@lanl.gov

Other Authors

Addis Fuhr − *Los Alamos National Laboratory, Los Alamos, New Mexico, and University of California, Los Angeles, Los Angeles, California*

Hyeong Jin Yun − *Los Alamos National Laboratory, Los Alamos, New Mexico*

Scott A. Crooker − *Los Alamos National Laboratory, Los Alamos, New Mexico;* orcid.org/0000-0001-7553-4718

Complete contact information is available at: https://pubs.acs.org/10.1021/acsnano.9b09181

Notes

The authors declare no competing financial interest.

ACKNOWLEDGMENTS

The studies of quantum dot photophysical and magneto-optical properties were supported by the Solar Photochemistry Program of the Chemical Sciences, Biosciences and Geosciences Division, Office of Basic Energy Sciences, Office of Science, U.S. Department of Energy. The research into the synthesis of the quantum dots was supported by the Laboratory Directed Research and Development program of Los Alamos National Laboratory (LANL) under project number 20190232ER. Measurements at the National High Magnetic Field Laboratory were supported by the National Science Foundation DMR-1644779, the State of Florida, and the U.S. Department of Energy. A.F. was supported by the LANL African American Partnership Program.

REFERENCES

(1) Jara, D. H.; Yoon, S. J.; Stamplecoskie, K. G.; Kamat, P. V. Size-Dependent Photovoltaic Performance of CuInS$_2$ Quantum Dot-Sensitized Solar Cells. *Chem. Mater.* **2014**, *26*, 7221−7228.

(2) Houck, D. W.; Assaf, E. I.; Shin, H.; Greene, R. M.; Pernik, D. R.; Korgel, B. A. Pervasive Cation Vacancies and Antisite Defects in Copper Indium Diselenide (CuInSe$_2$) Nanocrystals. *J. Phys. Chem. C* **2019**, *123*, 9544−9551.

(3) Li, L.; Daou, T. J.; Texier, I.; Kim Chi, T. T.; Liem, N. Q.; Reiss, P. Highly Luminescent CuInS$_2$/ZnS Core/Shell Nanocrystals: Cadmium-Free Quantum Dots for *In Vivo* Imaging. *Chem. Mater.* **2009**, *21*, 2422−2429.

(4) Jara, D. H.; Stamplecoskie, K. G.; Kamat, P. V. Two Distinct Transitions in Cu$_x$InS$_2$ Quantum Dots. Bandgap *versus* Sub-Bandgap Excitations in Copper-Deficient Structures. *J. Phys. Chem. Lett.* **2016**, *7*, 1452−1459.

(5) Panthani, M. G.; Akhavan, V.; Goodfellow, B.; Schmidtke, J. P.; Dunn, L.; Dodabalapur, A.; Barbara, P. F.; Korgel, B. A. Synthesis of CuInS$_2$, CuInSe$_2$, and Cu(In$_x$Ga$_{1-x}$)Se$_2$ (CIGS) Nanocrystal "Inks" for Printable Photovoltaics. *J. Am. Chem. Soc.* **2008**, *130*, 16770−16777.

(6) Koo, B.; Patel, R. N.; Korgel, B. A. Synthesis of CuInSe$_2$ Nanocrystals with Trigonal Pyramidal Shape. *J. Am. Chem. Soc.* **2009**, *131*, 3134−3135.

(7) Aldakov, D.; Lefrançois, A.; Reiss, P. Ternary and Quaternary Metal Chalcogenide Nanocrystals: Synthesis, Properties and Applications. *J. Mater. Chem. C* **2013**, *1*, 3756−3776.

(8) Berends, A. C.; Rabouw, F. T.; Spoor, F. C. M.; Bladt, E.; Grozema, F. C.; Houtepen, A. J.; Siebbeles, L. D. A.; de Mello Donega, C. Radiative and Nonradiative Recombination in CuInS$_2$ Nanocrystals and CuInS$_2$-Based Core/Shell Nanocrystals. *J. Phys. Chem. Lett.* **2016**, *7*, 3503−3509.

(9) van der Stam, W.; de Graaf, M.; Gudjonsdottir, S.; Geuchies, J. J.; Dijkema, J. J.; Kirkwood, N.; Evers, W. H.; Longo, A.; Houtepen, A. J. Tuning and Probing the Distribution of Cu$^+$ and Cu^{2+} Trap States Responsible for Broad-Band Photoluminescence in CuInS$_2$ Nanocrystals. *ACS Nano* **2018**, *12*, 11244−11253.

(10) Knowles, K. E.; Nelson, H. D.; Kilburn, T. B.; Gamelin, D. R. Singlet−Triplet Splittings in the Luminescent Excited States of Colloidal Cu$^+$:CdSe, Cu$^+$:InP, and CuInS$_2$ Nanocrystals: Charge-Transfer Configurations and Self-Trapped Excitons. *J. Am. Chem. Soc.* **2015**, *137*, 13138−13147.

(11) Hughes, K. E.; Ostheller, S. R.; Nelson, H. D.; Gamelin, D. R. Copper's Role in the Photoluminescence of Ag$_{1-x}$Cu$_x$InS$_2$ Nanocrystals, from Copper-Doped AgInS$_2$ ($x \sim 0$) to CuInS$_2$ ($x = 1$). *Nano Lett.* **2019**, *19*, 1318−1325.

(12) Nagamine, G.; Nunciaroni, H. B.; McDaniel, H.; Efros, A. L.; de Brito Cruz, C. H.; Padilha, L. A. Evidence of Band-Edge Hole Levels Inversion in Spherical CuInS$_2$ Quantum Dots. *Nano Lett.* **2018**, *18*, 6353−6359.

(13) van der Stam, W.; Berends, A. C.; Rabouw, F. T.; Willhammar, T.; Ke, X.; Meeldijk, J. D.; Bals, S.; de Mello Donega, C. Luminescent CuInS$_2$ Quantum Dots by Partial Cation Exchange in Cu$_{2-x}$S Nanocrystals. *Chem. Mater.* **2015**, *27*, 621−628.

(14) Xia, C.; Wu, W.; Yu, T.; Xie, X.; Van Oversteeg, C.; Gerritsen, H. C.; de Mello Donega, C. Size-Dependent Band-Gap and Molar Absorption Coefficients of Colloidal CuInS$_2$ Quantum Dots. *ACS Nano* **2018**, *12*, 8350−8361.

(15) Yarema, O.; Bozyigit, D.; Rousseau, I.; Nowack, L.; Yarema, M.; Heiss, W.; Wood, V. Highly Luminescent, Size- and Shape-Tunable Copper Indium Selenide Based Colloidal Nanocrystals. *Chem. Mater.* **2013**, *25*, 3753−3757.

(16) McDaniel, H.; Fuke, N.; Makarov, N. S.; Pietryga, J. M.; Klimov, V. I. An Integrated Approach to Realizing High-Performance Liquid-Junction Quantum Dot Sensitized Solar Cells. *Nat. Commun.* **2013**, *4*, 1.

(17) McDaniel, H.; Fuke, N.; Pietryga, J. M.; Klimov, V. I. Engineered CuInSe$_x$S$_{2-x}$ Quantum Dots for Sensitized Solar Cells. *J. Phys. Chem. Lett.* **2013**, *4*, 355−361.

(18) Kim, J.-Y.; Yang, J.; Yu, J. H.; Baek, W.; Lee, C.-H.; Son, H. J.; Hyeon, T.; Ko, M. J. Highly Efficient Copper−Indium−Selenide Quantum Dot Solar Cells: Suppression of Carrier Recombination by Controlled ZnS Overlayers. *ACS Nano* **2015**, *9*, 11286−11295.

(19) Du, J.; Du, Z.; Hu, J.-S.; Pan, Z.; Shen, Q.; Sun, J.; Long, D.; Dong, H.; Sun, L.; Zhong, X.; Wan, L.-J. Zn−Cu−In−Se Quantum Dot Solar Cells with a Certified Power Conversion Efficiency of 11.6%. *J. Am. Chem. Soc.* **2016**, *138*, 4201−4209.

(20) Voggu, V. R.; Sham, J.; Pfeffer, S.; Pate, J.; Fillip, L.; Harvey, T. B.; Brown, R. M.; Korgel, B. A. Flexible CuInSe$_2$ Nanocrystal Solar Cells on Paper. *ACS Energy Lett.* **2017**, *2*, 574−581.

(21) Panthani, M. G.; Stolle, C. J.; Reid, D. K.; Rhee, D. J.; Harvey, T. B.; Akhavan, V. A.; Yu, Y.; Korgel, B. A. CuInSe$_2$ Quantum Dot Solar Cells with High Open-Circuit Voltage. *J. Phys. Chem. Lett.* **2013**, *4*, 2030−2034.

(22) So, D.; Pradhan, S.; Konstantatos, G. Solid-State Colloidal CuInS$_2$ Quantum Dot Solar Cells Enabled by Bulk Heterojunctions. *Nanoscale* **2016**, *8*, 16776−16785.

(23) Meinardi, F.; McDaniel, H.; Carulli, F.; Colombo, A.; Velizhanin, K. A.; Makarov, N. S.; Simonutti, R.; Klimov, V. I.; Brovelli, S. Highly Efficient Large-Area Colourless Luminescent Solar Concentrators Using Heavy-Metal-Free Colloidal Quantum Dots. *Nat. Nanotechnol.* **2015**, *10*, 878−885.

(24) Bergren, M. R.; Makarov, N. S.; Ramasamy, K.; Jackson, A.; Guglielmetti, R.; McDaniel, H. High-Performance CuInS$_2$ Quantum Dot Laminated Glass Luminescent Solar Concentrators for Windows. *ACS Energy Lett.* **2018**, *3*, 520−525.

(25) Knowles, K. E.; Kilburn, T. B.; Alzate, D. G.; McDowall, S.; Gamelin, D. R. Bright CuInS$_2$/CdS Nanocrystal Phosphors for High-

Gain Full-Spectrum Luminescent Solar Concentrators. *Chem. Commun.* **2015**, *51*, 9129−9132.

(26) Sumner, R.; Eiselt, S.; Kilburn, T. B.; Erickson, C.; Carlson, B.; Gamelin, D. R.; McDowall, S.; Patrick, D. L. Analysis of Optical Losses in High-Efficiency $CuInS_2$-Based Nanocrystal Luminescent Solar Concentrators: Balancing Absorption *versus* Scattering. *J. Phys. Chem. C* **2017**, *121*, 3252−3260.

(27) Li, C.; Chen, W.; Wu, D.; Quan, D.; Zhou, Z.; Hao, J.; Qin, J.; Li, Y.; He, Z.; Wang, K. Large Stokes Shift and High Efficiency Luminescent Solar Concentrator Incorporated with $CuInS_2$/ZnS Quantum Dots. *Sci. Rep.* **2016**, *5*, 17777.

(28) Berends, A. C.; Mangnus, M. J. J.; Xia, C.; Rabouw, F. T.; de Mello Donega, C. Optoelectronic Properties of Ternary I-III-VI_2 Semiconductor Nanocrystals: Bright Prospects with Elusive Origins. *J. Phys. Chem. Lett.* **2019**, *10*, 1600−1616.

(29) Chuang, P.-H.; Lin, C. C.; Liu, R.-S. Emission-Tunable $CuInS_2$/ZnS Quantum Dots: Structure, Optical Properties, and Application in White Light-Emitting Diodes with High Color Rendering Index. *ACS Appl. Mater. Interfaces* **2014**, *6*, 15379−15387.

(30) Wang, T.; Guan, X.; Zhang, H.; Ji, W. Exploring Electronic and Excitonic Processes toward Efficient Deep-Red $CuInS_2$/ZnS Quantum-Dot Light-Emitting Diodes. *ACS Appl. Mater. Interfaces* **2019**, *11*, 36925−36930.

(31) Jiang, Y. R.; Cho, S. Y.; Shim, M. Light-Emitting Diodes of Colloidal Quantum Dots and Nanorod Heterostructures for Future Emissive Displays. *J. Mater. Chem. C* **2018**, *6*, 2618−2634.

(32) Pons, T.; Pic, E.; Lequeux, N.; Cassette, E.; Bezdetnaya, L.; Guillemin, F.; Marchal, F.; Dubertret, B. Cadmium-Free $CuInS_2$/ZnS Quantum Dots for Sentinel Lymph Node Imaging with Reduced Toxicity. *ACS Nano* **2010**, *4*, 2531−2538.

(33) Draguta, S.; McDaniel, H.; Klimov, V. I. Tuning Carrier Mobilities and Polarity of Charge Transport in Films of $CuInSe_xS_{2-x}$ Quantum Dots. *Adv. Mater.* **2015**, *27*, 1701−1705.

(34) Yun, H. J.; Lim, J.; Fuhr, A. S.; Makarov, N. S.; Keene, S.; Law, M.; Pietryga, J. M.; Klimov, V. I. Charge-Transport Mechanisms in $CuInSe_xS_{2-x}$ Quantum-Dot Films. *ACS Nano* **2018**, *12*, 12587−12596.

(35) Wang, H.; Butler, D. J.; Straus, D. B.; Oh, N.; Wu, F.; Guo, J.; Xue, K.; Lee, J. D.; Murray, C. B.; Kagan, C. R. Air-Stable $CuInSe_2$ Nanocrystal Transistors and Circuits *via* Post-Deposition Cation Exchange. *ACS Nano* **2019**, *13*, 2324−2333.

(36) Yamamoto, Y.; Yamaguchi, T.; Tanaka, T.; Tanahashi, N.; Yoshida, A. Characterization of $CuInS_2$ Thin Films Prepared by Sputtering from Binary Compounds. *Sol. Energy Mater. Sol. Cells* **1997**, *49*, 399−405.

(37) Yakushev, M. V.; Mudryi, A. V.; Gremenok, V. F.; Zalesski, V. B.; Romanov, P. I.; Feofanov, Y. V.; Martin, R. W.; Tomlinson, R. D. Optical properties and Band Gap Energy of $CuInSe_2$ Thin Films Prepared by Two-Stage Selenization Process. *J. Phys. Chem. Solids* **2003**, *64*, 2005−2009.

(38) Yakushev, M. V.; Martin, R. W.; Mudryi, A. V. Diamagnetic Shifts of Free Excitons in $CuInS_2$ in Magnetic Fields. *Appl. Phys. Lett.* **2009**, *94*, 042109.

(39) Fuhr, A.; Yun, H. J.; Makarov, N. S.; Li, H.; McDaniel, H.; Klimov, V. I. Light-Emission Mechanism in $CuInS_2$ Quantum Dots Evaluated by Spectral Electrochemistry. *ACS Photonics* **2017**, *4*, 2425−2435.

(40) Li, L.; Pandey, A.; Werder, D. J.; Khanal, B. P.; Pietryga, J. M.; Klimov, V. I. Efficient Synthesis of Highly Luminescent Copper Indium Sulfide-Based Core/Shell Nanocrystals with Surprisingly Long-Lived Emission. *J. Am. Chem. Soc.* **2011**, *133*, 1176−1179.

(41) Rice, W. D.; McDaniel, H.; Klimov, V. I.; Crooker, S. A. Magneto-Optical Properties of $CuInS_2$ Nanocrystals. *J. Phys. Chem. Lett.* **2014**, *5*, 4105−4109.

(42) Zang, H.; Li, H.; Makarov, N. S.; Velizhanin, K. A.; Wu, K.; Park, Y.-S.; Klimov, V. I. Thick-Shell $CuInS_2$/ZnS Quantum Dots with Suppressed "Blinking" and Narrow Single-Particle Emission Line Widths. *Nano Lett.* **2017**, *17*, 1787−1795.

(43) Fuhr, A. S.; Sautet, P.; Alexandrova, A. N. Heterogeneity in Local Chemical Bonding Explains Spectral Broadening in Quantum Dots with Cu Impurities. *J. Phys. Chem. C* **2019**, *123*, 5705−5713.

(44) Pinchetti, V.; Lorenzon, M.; McDaniel, H.; Lorenzi, R.; Meinardi, F.; Klimov, V. I.; Brovelli, S. Spectro-Electrochemical Probing of Intrinsic and Extrinsic Processes in Exciton Recombination in I−III−VI_2 Nanocrystals. *Nano Lett.* **2017**, *17*, 4508−4517.

(45) Suzuki, A.; Shionoya, S. Mechanism of the Green-Copper Luminescence in ZnS Crystals. I. Direct Evidence for the Pair Emission Mechanism. *J. Phys. Soc. Jpn.* **1971**, *31*, 1455−1461.

(46) Kröger, F. A.; Vink, H. J. Relations between the Concentrations of Imperfections in Crystalline Solids. *Solid State Phys.* **1956**, *3*, 307−435.

(47) Furdyna, J. K. Diluted Magnetic Semiconductors. *J. Appl. Phys.* **1988**, *64*, R29−R64.

(48) Pandey, A.; Brovelli, S.; Viswanatha, R.; Li, L.; Pietryga, J. M.; Klimov, V. I.; Crooker, S. A. Long-Lived Photoinduced Magnetization in Copper-Doped ZnSe-CdSe Core-Shell Nanocrystals. *Nat. Nanotechnol.* **2012**, *7*, 792−797.

(49) Bussian, D. A.; Crooker, S. A.; Yin, M.; Brynda, M.; Efros, A. L.; Klimov, V. I. Tunable Magnetic Exchange Interactions in Manganese-Doped Inverted Core−Shell ZnSe−CdSe Nanocrystals. *Nat. Mater.* **2009**, *8*, 35.

(50) Xie, R.; Rutherford, M.; Peng, X. Formation of High-Quality I-III-VI Semiconductor Nanocrystals by Tuning Reltive Reactivity of Cationic Precursors. *J. Am. Chem. Soc.* **2009**, *131*, 5691−5697.

(51) Norris, D. J.; Bawendi, M. Measurement and Assignment of the Size-Dependent Optical Spectrum in CdSe Quantum Dots. *Phys. Rev. B: Condens. Matter Mater. Phys.* **1996**, *53*, 16338−16346.

(52) Klimov, V. I.; Baker, T. A.; Lim, J.; Velizhanin, K. A.; McDaniel, H. Quality Factor of Luminescent Solar Concentrators and Practical Concentration Limits Attainable with Semiconductor Quantum Dots. *ACS Photonics* **2016**, *3*, 1138−1148.